Standoff detection of biological aerosols by UV-laser induced fluorescence

Gunnar Rustad and Øystein Farsund

Norwegian Defence Research Establishment (FFI)

31 October 2008

FFI-rapport 2008/02025

111602

P: ISBN 978-82-464-1650-2
E: ISBN 978-82-464-1651-9

Keywords

Avstandsdeteksjon

Biologiske stridsmidler

UV fluorescens

Lidar

UVLIF

Approved by

Hans Christian Gran	Project manager
Jan Ivar Botnan	Director

English summary

This report describes the experimental biolidar developed at FFI during the period 2005-2007 to detect biological aerosols. The biolidar is based on ultraviolet laser induced fluorescence, in which ultraviolet light is used to induce fluorescence in aerosols. It turns out that aerosols with biological content emit fluorescence when excited at certain wavelengths, e.g. 355 nm, which was used in this work, and this can be used to distinguish biological aerosols from other aerosols.

The biolidar was built with commercially available components, and in the initial lidar design described here, also commercial software for data acquisition was used. In the design of the lidar, it was chosen to keep the elements simple and – if possible – with better performance than expected necessary. This way it will be possible to reduce the performance of the lidar artificially to get an estimate of the performance needed in a final design. The design of the lidar is described and explained, and initial results are shown.

Sammendrag

Denne rapporten beskriver et eksperimentelt instrument som kalles *biolidar* og som er utviklet ved FFI i perioden 2005-2007. Biolidaren har som formål å oppdage aerosoler med biologisk innhold for å kunne gi tidlig oppdagelse av utslipp av biologiske stridsmidler. Biolidaren baseres på ultrafiolett laserindusert fluorescens hvor ultrafiolett laserlys benyttes til å indusere fluorescens i aerosoler. Det viser seg at aerosoler med biologisk innhold fluorescerer når de eksiteres på bestemte bølgelengder, for eksempel 355 nm, som er brukt i dette arbeidet, og at dette kan brukes for å skille dem fra andre aerosoler. Biolidaren ble bygget med kommersielt tilgjengelige komponenter og i den første utgaven som rapporteres her, er det også benyttet kommersielle dataprogrammer til for eksempel datainnhenting og styring av instrumentene.

I utviklingen av biolidaren har det blitt lagt vekt på å holde designet enkelt og – hvis mulig – med bedre ytelse enn hva som er forventet nødvendig. Grunnen til dette er at ytelsen til biolidaren da kan kunstig reduseres for å finne ut hva som trengs i senere utviklinger. I rapporten er biolidaren beskrevet og prinsipper og ulike valg er forklart. I tillegg er eksempler på resultater med instrumentet vist.

Contents

1 Introduction

A prototype instrument for standoff detection of biological aerosols has been built within the frames of the FFI project 1001 “ARBC forsvar”. This report describes the design of and technological background for this instrument.

The objective of standoff detection is to enable early warning in case of a biological warfare agent (BWA) attack, in order to bring preventive measures into action before contamination. Standoff detection should be seen as part of a detection system that also includes other detectors that e.g. can confirm and investigate a detected threat further.

1.1 Candidate technologies

There are two basic requirements that should be fulfilled for a lidar to work properly:

- The object to be examined must have a signature of some kind that is different from the background and other objects
- This signature should be in a spectral band with good atmospheric transmission

One way of detecting biological aerosols at a distance without contaminating the instrument is based on ultraviolet laser induced fluorescence (UVLIF). A UV laser pulse is fired at the biological aerosol, in which certain biological molecules are excited and fluoresces, i.e. reemits light at lower frequencies, which is then measured by the instrument. The spectral content of this fluorescence depends on the substance that is fluorescing, and can thus be used for detection.

In another, less technologically mature approach, elastic scattering at infrared laser wavelengths is measured. Different substances have different spectral signatures of this back-scatter, and this is used for detection. This approach typically requires a large (>10) different laser wavelengths. There is also one approach that study how the polarized laser light is depolarized in the back-scatter process at multiple laser wavelengths.

There are also other technological approaches to standoff detection of biological aerosols. These are at a very early stage, and include laser-induced breakdown spectroscopy with very energetic short-pulse lasers, passive hyperspectral imaging, and terahertz (THz) spectroscopy [1].

In the instrument described herein, the detection principle is based on UVLIF.

1.2 Literature overview

There has been a substantial research effort on standoff detection of biological aerosols in Canada, United Kingdom and USA, mostly financed through the respective countries’ ministries of defence (MoD). More recently, France and Norway (FFI) also have started activities in this field, and there are also emerging efforts in Sweden, Germany, the Netherlands, and Slovakia. There is also an ongoing international project under the EU programme lead by the French

company Cilas. On the other hand, several countries have studied contact-free point detection, which in many cases is based on the same detection principles. Most countries base their instruments on the UVLIF technology, while the infrared approach described above is being developed in the USA. The UVLIF technology is also studied in USA, and a first generation standoff detection system for operational use has recently been developed[1].

Much of the work done in this field is only reported at conferences or through e.g. NATO meetings. A comprehensive overview of the current effort can be found in the proceedings from the 6th and 7th *Joint Conference on Standoff Detection for Chemical and Biological Defence* [1, 2], which is considered the main conference in this field. Also, one of the seminars in the SPIE conference *Defence and Security* deals with CBRN defence, and useful information can be found even in the proceedings from this conference series [3]. In Table 1.1, a simplified overview of the current research is listed

Table 1.1 Overview of current research efforts

Country	Approach	Laser	Detection
GBR	UVLIF	266 nm	10 channel
CAN	UVLIF	355 nm	>100 channel
USA	IR Backscatter	10 µm (19)	1 channel
USA	IR Depolarization	1+1.5+3 µm	2 polarizations
USA	UVLIF	355 nm	2 channel
Norway	UVLIF	355 nm	>100 channel
France	UVLIF	280-340 nm	1 channel
EU/France	UVLIF	280 + 355 nm	8 channel

1.3 Overview of the report

In Chapter 2, the fundamental physical processes that form the base for the measurement principle are briefly discussed. A model for measuring biological aerosol concentration by means of UVLIF is presented in Chapter 3, and the details of the prototype instrument are described in Chapter 4. Laser safety issues are discussed in Chapter 5, and examples of results with the instrument are shown in Chapter 6, before conclusions are drawn.

2 Principle of detection

The ultraviolet laser induced fluorescence (UVLIF) technique is the basis of this work, and is described in Section 2.1. First, a brief description of the principle of function for the developed instrument is given.

The instrument consists of an ultraviolet laser delivering short (5 nanosecond), but energetic pulses, and a telescope to collect the return radiation and to focus in onto the detection system.

[1] Joint Biological Standoff Detection System (JBSDS) made by SESI (www.sesi-md.com)

Such an instrument is frequently called a *lidar* (LIght Detection And Ranging). When the collimated ultraviolet laser pulse is sent through a cloud of biological aerosols, part of the light is scattered backwards without loss of energy (elastic scattering), and part of the light is absorbed by biological molecules in the aerosols, which subsequently emit light at lower frequencies than the excitation (laser) frequency. This is frequently referred to as inelastic scattering or fluorescence. The aerosol cloud scatters light in all directions, and some of the scattered light is collected by the telescope. In the detection system, the collected light is spectrally separated such that the elastically scattered light impinges a fast detector (photomultiplier tube, PMT), and the lower frequency light (fluorescence signal) is directed into a spectrograph and detected by a gated camera. The PMT measures the time of flight for the light, yielding the measurement range distance to and depth of the cloud of interest. These parameters are used to control the camera gating, in order to collect light from the region of interest. The camera records the spectral content of the fluorescence signal.

The instrument needs optical visibility and line of sight throughout the operating range. In low visibility conditions such as fog or heavy precipitation other techniques should be employed, if at all BWA releases are likely under such conditions. Naturally occurring biological molecules, *e.g.* pollen and fungi dispersed in the air, represent a challenge as these molecules also emit fluorescence when being hit by the UV laser pulse. Another challenge is the vegetation, which also has a strong fluorescence. In general, a ground based instrument can fairly easy deal with a fluorescing background, as the line of sight is parallel to the ground. An airborne instrument, on the other hand, will constantly face this challenge as it is looking toward the ground, usually covered by vegetation. Airborne measurements are additionally complicated because a potential BWA cloud most likely is very close to the ground. Moreover, a potential cloud of BWA will most likely spread in the horizontal direction enabling a horizontal-looking ground-based lidar to probe a significant part of the cloud, thus increasing the measured signal. Of these reasons, a UVLIF-based instrument may be less suited for airborne operation.

2.1 Fluorescence

Fluorescence is a special case of luminescence – the emission of light not solely related to the temperature of the luminous object. Absorption of incident radiation in a molecule leads to an electronic transition within the molecule. The molecule can then relax back to its original state (normally the ground state) through several processes. In some cases, this relaxation process includes the emission of a photon, which is known as fluorescence. Other relaxation processes, like vibrational transitions, interstate transfer, or loss of energy through molecular collisions, do not include emission of photons (nonradiative). In the case of fluorescence, this often occurs in combination with nonradiative processes, thus reducing the energy (i.e. frequency) of the emitted photon. This may lead to a spectrum of the fluorescence that is characteristic for a particular molecule. The decay time of fluorescence is typically in the range from nanoseconds to milliseconds [4, 5]. Not all molecules will emit fluorescence, and for those who do, the fluorescence often depends strongly on the excitation frequency, as there may be certain molecular transitions that, when excited, give rise to fluorescence. Of the molecules that are

typical to biological aerosols, a few are sources to strong fluorescence, and are described in the following.

2.2 Fluorophores

In the context of standoff detection of biological aerosols, two molecules are of particular interest; NADH and tryptophan. NADH is the reduced form of nicotinamide adenine dinucleotide (NAD^+), and is important in cell respiration and hence metabolism. NADH is therefore present in bacteria and other living cells, but to a lesser degree in spores or viruses. Tryptophan is an amino acid,[2] and thus present in all biological material, including viruses. Also other biological molecules emit fluorescence, but to a lesser degree, and less relevant for standoff detection. The absorption and fluorescence spectra of the relevant substances are shown below. A more through overview of different fluorescent substances can be found in an internal report [6].

2.2.1 Tryptophan

Tryptophan is an amino acid, i.e. one of the building blocks in the protein synthesis that occur in cells. Tryptophan has absorption peaks at 230 nm and 280 nm, the latter being of particular interest in standoff detection applications. When excited at 280 nm, tryptophan emits fluorescence with a peak around 350 nm. Tryptophan can also be excited at other UV wavelengths, but with reduced fluorescence intensity as a possible result. For example, excitation with the common laser wavelength at 266 nm would result in about 25% of the fluorescence when excited at 280 nm. In Figure 2.1, the absorption spectra of the three fluorescing amino acids, tryptophan, tyrosine and phenylalanine, are shown. In Figure 2.2, the emission spectrum for tryptophan is shown after excitation with 266 nm.

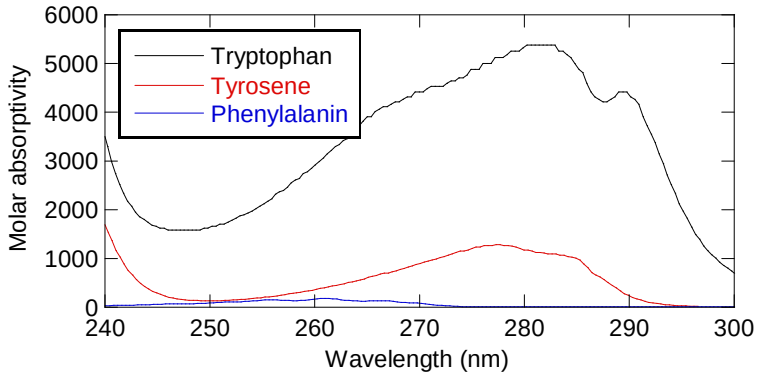

Figure 2.1 Absorption spectra for tryptophan, tyrosine and phenylalanine (spectra taken from [7])

[2] (*S*)-2-Amino-3-(1H-indol-3-yl)-propionic acid, with chemical formula $C_{11}H_{12}N_2O_2$

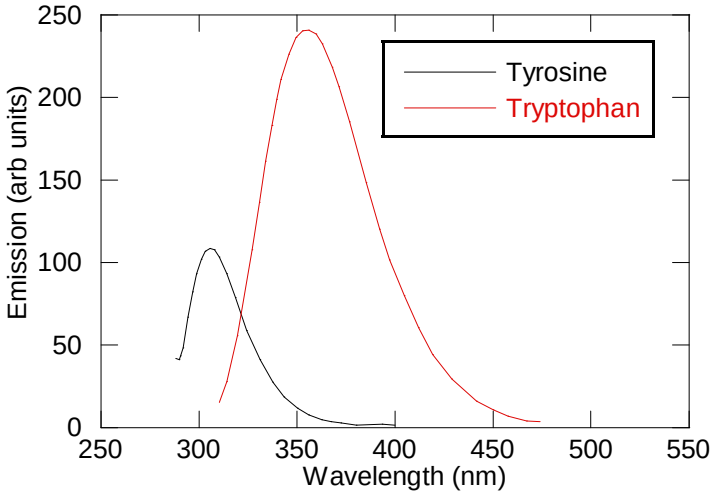

Figure 2.2 Fluorescence spectrum for tryptophan and tyrosine excited at 266 nm (spectra taken from [8])

2.2.2 NADH

NADH is a protein and an important part of the synthesis of ATP, which is the universal energy carrier for cells. Therefore, NADH will be present in all living cells. NADH is excited around 340-350 nm, and has an emission peak around 450 nm, as can be seen in Figure 2.3.

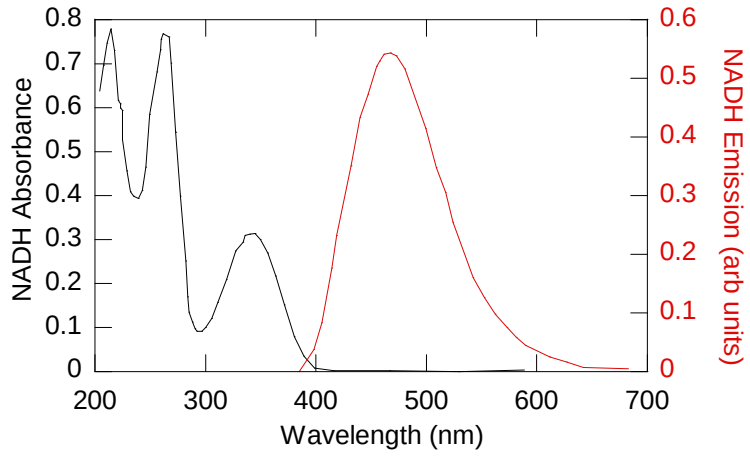

Figure 2.3 Picosecond absorption spectroscopy of a 5 x 10^{-5} M aqueous NADH solution (data taken from [9])

2.2.3 Other fluorescent molecules

There are two other molecules that may be relevant for UV laser induced fluorescence; flavins and dipiclonic acid.

The source of flavins is the vitamin riboflavin. The peak absorption wavelength is ~450 nm, and the emission peak is at ~550 nm.

Dipiclonic Acid (DPA) is formed during sporification. Its absorption and emission spectra resembles that of tryptophan, but it is weak and is expected to be completely masked by emission from tryptophan.

2.3 Time-resolved spectroscopy

In time-resolved spectroscopy both the emission spectra and the lifetimes of the spectral components are measured. This can be a powerful tool in laboratory measurements. However, as typical decay times are typically sub-nanosecond up to a few tens of nanoseconds, such time variations will be masked by the difference in time of flight for the different parts of an aerosol cloud (a 10 m thick cloud will return a ~60 ns long signal). Therefore, time-resolved spectroscopy is not fit for the standoff detection measurements in this work.

3 Instrument design

3.1 Model

The factors that influence on the detection process in a lidar can be collected in the so-called *lidar equation.* This is given below, and describes the spectrally distributed inelastic scattering, by a single type of inelastic scatterer, collected by the instrument (before the ICCD camera) [5, 10, 11]

$$\frac{dE}{d\lambda_{IS}}(\lambda,\lambda_0) = \underbrace{E_0(\lambda_0)}_{\text{Energy delivered}} \cdot \underbrace{\xi(r)\frac{A_0}{r^2}}_{\text{Geometry factors}} \cdot \underbrace{t_{oe}(\lambda_0)t_{oc}(\lambda)}_{\text{Transmission in optics}} \cdot \underbrace{t_{ac}(\lambda_0,r)t_{ac}(\lambda,r)}_{\text{Atmospheric transmission}} \cdot \underbrace{\Delta r N_{IS}(r)}_{\text{Scatter column thickness}} \cdot \underbrace{\frac{d^2\sigma}{d\Omega d\lambda_{IS}}(\lambda_0,\lambda)}_{\text{Scatter properties}} \tag{3.1}$$

Here, λ_0 is the laser wavelength and λ is the scattered wavelength, r is the distance between the lidar and the aerosols, A_0 is the area and ξ is the obscuration factor of the collecting optics (telescope), and $\Delta r N_{IS}$ is the area density of the inelastic scatterers (density times average column thickness). The last term is the scatter cross section of the particle. The geometry factors have been treated extensively with an optics simulation program (Zemax, [12]) and are described in a separate report [13]. The transmission in optics and the response function of the detection system is treated in Section 3.2.4.

3.2 Atmospheric transmission

The factors that influence most strongly on the atmospheric transmission is absorption in ozone for wavelengths below ~300 nm, and the concentration of naturally occurring aerosols. In Figure 3.1, the calculated horizontal transmission through 1 km for different ozone concentrations and for a standard atmosphere with different aerosol content. We notice that the transmission of 266 nm varies strongly with ozone concentration, from 53% at the concentration in the US standard model, and down to 9% for a higher, but not unrealistic concentration under certain conditions [14]. We also notice that the effect of ozone is much less at 280-290 nm, which is the wavelength

region where the absorption in tryptophan is considerably stronger than at 266 nm. The transmission in the 350-500 range varies by a factor of 2-3 from a "hazy" to a clear day, owing to scattering losses of the naturally occurring aerosols. The calculations were performed with Modtran [15].

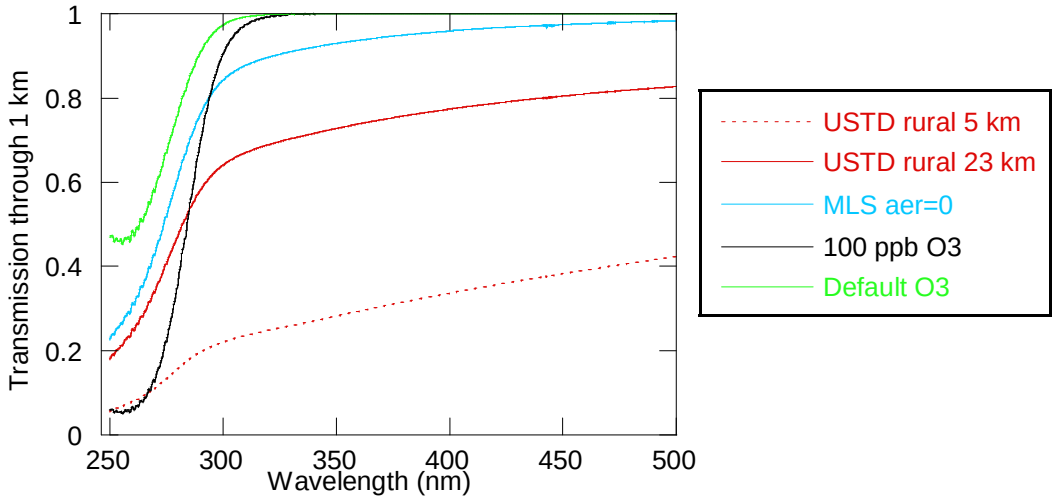

Figure 3.1 *Calculated transmission through 1 km for different conditions using Modtran [15]. The red and blue curves are for US standard atmosphere with different aerosol content; blue is none, solid red is 23 km visibility (clear day), and red dotted is for 5 km visibility ("hazy" day). Black and green curves are the ozone transmission curves; the green is for the standard concentration in the model (~50 ppb) and the black is for 100 ppb ozone which can sometimes be present in urban environments and during seasonal variations in rural environments [14]*

3.3 Scatter cross section

There exist some published values for the fluorescence scatter cross section of substances relevant for this work. They are, however, hard to compare as the substances may have been prepared differently or different excitation wavelengths have been used. In Table 3.1, different published values for *Bacillus Globii* (BG), a common simulant for *Bacillus Antracis* (Anthrax), are listed. The listed values are for the total fluorescence and for *unwashed* bacteria.[3] Some measurements have been performed on BG in a liquid suspension whereas others have measured on dry bacteria. It has been seen that the fluorescence is significantly stronger for aerosol particles in liquid suspension [16] (a factor of ~5), but the effect is not fully understood. All cross sections have been converted to the same units for comparison, i.e. cross section per solid angle (cm^2/sr). Stephens [17] measured the fluorescence cross section for BG spores and vegetative cells with 280 nm excitation. He found that at the emission cross section to be about an order of magnitude larger for vegetative cells than for spores ($2.25 \cdot 10^{-12}$ vs. $3 \cdot 10^{-13}$ cm^2/sr).

[3] Unwashed spores or bacteria may have remains of the growth medium at the surface, and this will also contribute to the fluorescence, contrary to washed bacteria where this has been washed off. Unwashed BG is most commonly used during field tests etc.

The large variation in measured cross sections indicate that the measurements are difficult to perform and that the result depends strongly on e.g. sample preparation. The published values should therefore be treated with caution when used in simulations.

Table 3.1 Published fluorescence cross sections for unwashed BG spores

Exc. wavelength nm	Cross section cm^2/sr-particle	Dry/Wet	Reference
266	$1.8 \cdot 10^{-12}$	Dry	[18]
280	$3 \cdot 10^{-13}$	Dry	[17]
280	$1.3 \cdot 10^{-12}$	Dry	[19]
355	$6 \cdot 10^{-11}$	Wet	[10]
355	$6.7 \cdot 10^{-13}$	Dry	[18]
360	$2.1 \cdot 10^{-12}$	Dry	[19]

3.4 Photon return estimates

Using the values presented in the previous section, it is possible to estimate the return lidar signal with the lidar equation in section 3.1. If transmission losses in optics and the atmosphere are disregarded (i.e. transmission = 1), a simplified version of the lidar equation (3.1) is found, giving the total fluorescence energy at the receiver,

$$E_{\Sigma fluor} = E_0(\lambda_0)\frac{A_0}{r^2}\Delta r N_{IS}(r)\int \frac{d^2\sigma}{d\Omega d\lambda_{IS}}(\lambda_0,\lambda)d\lambda_{IS}, \tag{3.2}$$

where the value of the integral is the value listed in column 2 in Table 3.1. The formula is now simply the fluorescence cross section multiplied with the number of scattering particles multiplied with the solid angle of the receiver. For a 20 m thick aerosol cloud with 1000 BG particles per liter of air at 1000 m distance, there will be ~$1.4 \cdot 10^6$ particles in a laser beam with 0.3 mrad divergence. With a 250 mm diameter optical telescope, the total fluorescence signal at the focal plane of the collecting optics will then be ~$7 \cdot 10^{-14}$ of the laser pulse energy, assuming a fluorescence cross section of $1 \cdot 10^{-12}$ cm^2/sr. For 100 mJ laser energy, approximately 15000 fluorescence photons will then be collected by the telescope. If the detection system has 50 spectral channels, ~300 photons will on the average be recorded in each channel if losses in the detection system are disregarded.

For comparison, ambient light owing to Rayleigh scatter in day-light conditions is 1.75 mW/cm^2sr for the 0.4-0.7 μm band [20, p144]. If we assume that the lidar has a 100 m gate width (see next chapter for explanation of the lidar), this corresponds to ~2000 photons per 7 nm wide channel during the exposure time. This illustrates the major challenge with ultraviolet laser induced fluorescence systems, and also why their performance is reduced with increasing ambient light level.

4 Description of Lidar

4.1 Overview

A breadboard based lidar was developed in this work. This is constituted by a UV laser and a detection system. Only commercial-off-the-shelf (COTS) components were used, and the different parts will be described in the following. The laser light was sent out on-axis to the telescope with a steering mirror. The alternative approach with off-axis geometry is generally not suitable in this application because of the narrow laser beam and field of view of the detection system which would give overlap only at a limited range of distances. The detection system consists of a telescope which collects and focuses the light onto a spectrograph which spectrally resolves the light onto an intensified camera. The elastically backscattered laser light is reflected by a dichroic beam splitter and onto a photo multiplying tube (PMT). A regular camera can also be inserted in the beam to check on the focusing of the detection system.

The main components are listed in Table 4.1, and the lay-out on the optical table is shown in Figure 4.1 and 4.2. The lidar is mounted on a 2.5 x 4 foot (750 x 1200 mm) breadboard. The total system weighs about 100 kg. In the following sections, we describe the different parts of the lidar in detail, and explain the considerations and requirements for each component.

Table 4.1 List of main components in the lidar

Component	Supplier	Model
Gated, intensified CCD camera	Andor	DH720-18H-83
Frequency tripled NdYAG laser	Quantel	Brilliant B
Newtonian celestial telescope	Orion Optics	Europa 250f4.8
Photo multiplier tube	Hamamatsu	R3810

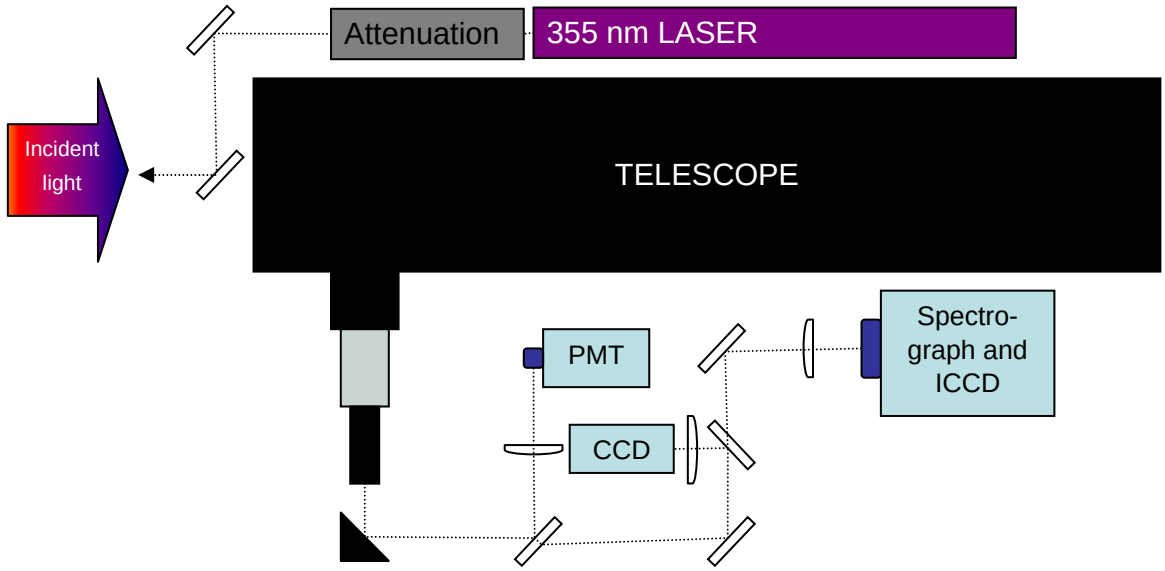

Figure 4.1 Sketch of the layout of the breadboard-based lidar

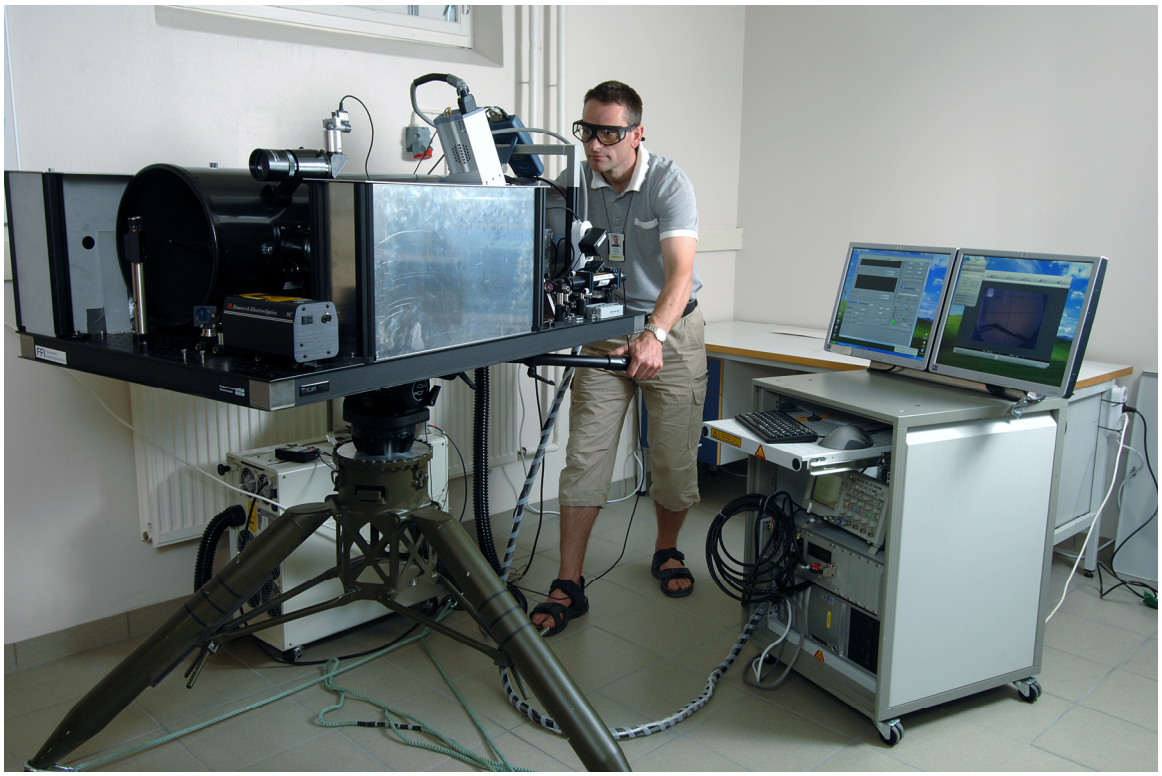

Figure 4.2 The FFI biolidar including the laser power supply (behind the tripod) and the control unit (to the right of the lidar)

4.2 Description of lidar parts

4.2.1 Laser

There are a few considerations that need to be taken into account when choosing the laser for this experiment. These are pulse energy, pulse length, pulse repetition rate, wavelength, beam quality, ruggedness and operating stability, and weight.

- Laser pulse energy: Should be as high as possible, but weaker pulses can be compensated by integration over more pulses. In this case, the pulse rate should be higher. This would, however, lead to a weaker signal to background ratio as the recorded background will increase. In the experiments reported here, we received strong fluorescence returns with 50-100 mJ of laser pulse energy.
- Laser pulse length: The pulse length determines the longitudinal resolution, 6 ns ↔1 m. Typical Q-switched pulse length are in the range 1-100 ns which should be sufficient.
- Laser pulse repetition rate: Since the measurement process typically requires averaging over a large number of pulses, the pulse repetition rate should be as high as possible that could be recorded by the detection system
- Laser wavelength: The easily available laser wavelength are the third and fourth harmonics of the Nd:YAG laser at 355 nm and 266 nm, respectively. These wavelength are also suitable (but not optimal) for exciting NADH and Tryptophan, respectively.

- Beam quality: The laser beam divergence should not be larger than the detection system field of view as the laser energy outside this is wasted in the detection process. For an 8 mm diameter beam at 355 nm, the ($FWe^{-2}M$) divergence of a beam of perfect beam quality is only 57 µrad, thus even beam qualities at $M^2 \sim 5$ (five times the perfect divergence) can be accepted within the ~0.3 mrad FOV of the detection system. Additionally, a poorer beam quality can be compensated by a larger beam – the divergence of a 10 mm diameter perfect beam is 45 µrad.
- Ruggedness and stability: Since the laser is a principal part of the lidar, the laser must have stable operation under the various conditions the lidar may be operated under
- Weight: The weight of the laser is important since it is a part of a mobile system. This also apply to the power supply, but to a lesser degree

The laser used in this work is a Quantel Brilliant B with 10 Hz pulse rate, and capability of 200 mJ at 355 nm and 40 mJ at 266 nm. In the work reported here, only the 355 nm output was used. The pulse rate of the laser is not optimal for the experiments, but most lasers with similar pulse energies at higher pulse rates are significantly larger and thus less suited for a mobile system.

The laser has a relatively long startup time – typically 45 minutes from startup to stable operation, but once it reached this operating regime, it worked reasonably well even in outdoor experiments with temperatures around freezing.

The far field of the 355 nm laser beam is elliptical with full divergence of ~0.2 x 0.8 mrad and the axes of the ellipse made an angle of about 30º to the horizontal plane. Since we use a slit at the entrance of the spectrograph, the field of view of the detection system is different in the horizontal and vertical directions, and in a late modification we used a dove prism to rotate the far field of the laser to match the shape of the spectrograph FOV.

The 355 nm laser beam exiting the laser is divergent and a small adjustable beam expander was used to control the collimation of the laser beam. This consisted of two AR-coated lenses with focal lengths of -100 mm and 125 mm, respectively, and the distance between the lenses could be adjusted around 25 mm.

4.2.2 Telescope

The telescope collects and focuses the scattered light onto the detectors. Below we have listed factors that need to be taken into account.

- Wavelength throughput: Needs to have high transmission at all relevant wavelengths. This may exclude telescope designs that include correction phase plates as these tend to have poor UV transmission. For 266 nm excitation, the reflectivity of the aluminum mirrors may not be good enough.
- Diameter: The larger diameter, the more light is collected
- f#: The f# is a measure for the inverse of the maximum divergence in an optical system, given by f/D, where D is the diameter of the optics and f is the focal length. The f# should be matched to that of the rest of the detection system, in particular the spectrograph. If the

f# of the telescope is smaller than that of the spectrograph, some of the collected light will not transmit the spectrograph. If the f# is too large, the resolving power of the spectrograph may not be exploited. Matching of the f# can be achieved with additional lenses between the telescope and the spectrograph.

- Size: Different telescope geometries have different sizes. The main alternatives are a Newtonian or a Cassegrian geometry. The main difference is that a Newtonian telescope has one curved mirror while a Cassegrian has two. The Cassegrian telescope is therefore significantly shorter than a Newtonian telescope with similar diameter. However, commercial telescopes based on the Cassegrian geometry often have a correcting phase plate with limited transmission in the UV, and are therefore not suited for UV-detection. Another difference is that, owing to the shorter length of the telescope, the secondary mirror of the Cassegrian telescope will be significantly larger, thus reducing the effective aperture of the telescope. A Newtonian telescope has been used in this work, but a Cassegrian telescope will be considered in future upgrades of the system.

4.2.3 PMT

In this work, a separate PMT has been used for two main reasons:

- The elastic scatter is much (a factor of ~10000) stronger than the fluorescence. Therefore, we choose to split this wavelength off the detection path and detect it separately
- The ICCD camera gives an integral over a designated time. This time should match the signal from the particle cloud, and it can be obtained by using PMT in a separate detection loop.

The requirements for the PMT and the amplification circuit are

- Sufficient bandwidth to give desired longitudinal resolution. Here, we have used 150 MHz, which corresponds to ~1 m resolution.
- Sufficient sensitivity at the laser wavelength
- At the laser wavelength, there is considerable scattering from naturally occurring aerosols. This scatter will be strongest close to the lidar, mainly because of the solid angle of the detection system. A possibility to gate the PMT to avoid this large background is therefore desirable.

It turned out that the main challenge for the PMT is to have a low noise/high bandwidth amplification of the PMT signal. We have used a Hamamatsu R3810 PMT with 10-20% quantum efficiency 200-450 nm, a C4900-01 power supply, and an M8879 amplifier with 150 MHz bandwidth. We did not find power supplies that were capable of a nanosecond-controlled gating of the PMT and have therefore not used gating in these experiments.

The size of the PMT-cathode is 3 x 4 mm^2. This gives the PMT a much larger FOV than is covered by the laser beam, but since the PMT signal is time resolved and thus strongly depend on the laser pulse, this is judged to be of less importance to the performance of the lidar.

4.2.4 Spectrograph and ICCD

A spectrograph is used to spectrally resolve the return signal. This is of Czerny-Turner geometry and consists of an entrance slit, a collimating mirror, a grating, and a focusing mirror imaging the width of the slit onto the exit face of the spectrograph, as shown in Figure 4.3. In the direction parallel to the slit, there is no imaging. Therefore, the camera can be operated in the Full Vertical Binning mode since the direction parallel to the slit is vertical on the camera.

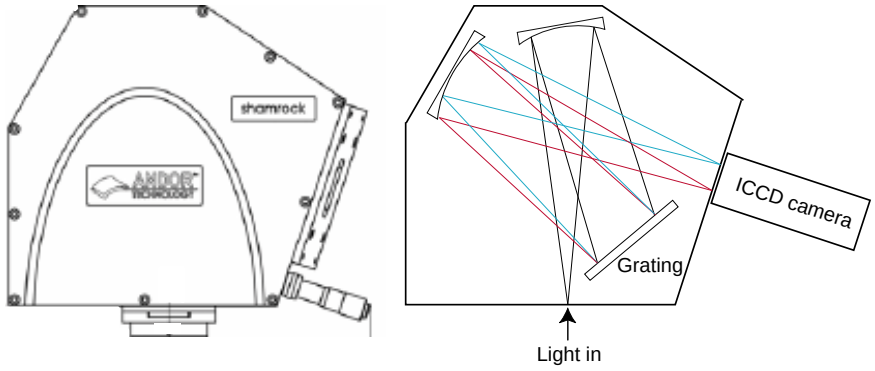

Figure 4.3 Geometry of the spectrograph

The spectral resolution of a spectrograph is given by

$$\Delta\lambda = D\frac{d\lambda}{dx} = \frac{D\cos\beta}{k \cdot f \cdot g}, \tag{4.1}$$

where λ is the wavelength, $\Delta\lambda$ is the resolution in wavelength, D is the width of the slit, β is the angle between the grating normal and the exit beam, k is the diffraction order, f is the focal length of the system (assumed to have magnification = 1 in the direction perpendicular to the slit), and g is the grating frequency in rules/mm. The dispersion of the spectrograph, $d\lambda/dx$, is a measure of how fast the wavelength changes with distance at the exit aperture of the spectrograph, and is often stated in the specifications of the instrument.

The spectrograph used in this work has a 200 µm wide slit, f = 163 mm and f# = 3.6, and a grating with 300 rules/mm with a 500 nm blaze angle (wavelength of maximum diffraction efficiency). The diffraction order of maximum efficiency is k = 1. The dispersion with this grating is stated to be 19.9 nm/mm (which corresponds to an angle β =13.3º). Using these values, we find that $\Delta\lambda$ = 4 nm.

The light at the exit face of the spectrograph is captured by the ICCD camera. The pixel size (or rather center-to-center distance of the pixels) of this camera is 26 µm (18 mm/696 pixels). Since the spectrograph has a magnification of 1 in the direction perpendicular to the slit and the 200 µm width of the slit is the limiting resolution of the system, it turns out that the camera sampling can be reduced by a factor of 7.7 without reducing the information available in the system. This can be done by horizontal binning blocks of 7 pixels.

The camera used in this work is an Andor iStar DH720-18H. This is an intensified CCD camera with 256 x 696 pixels, it has possibility of down to 100 ns gating, the gain can be adjusted from 0-500, and the quantum efficiency of the cathode is approximately 25% at 400 nm (i.e. 25% of the photons at this wavelength results in a free electron which is amplified a factor 0-500 in the multichannel plate before they hit the florescent anode screen. This light from this screen is collected by a CCD camera. The curve for the quantum efficiency of the camera cathode and the spectrograph grating is shown in Figure 4.4.

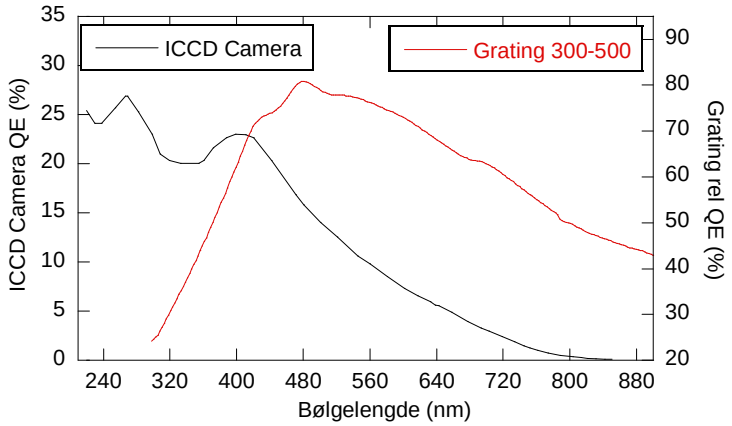

Figure 4.4 Quantum efficiency curves for the camera and the grating, as provided by the manufacturer (Andor, [21])

It should be noted that in Figure 4.4 the grating quantum efficiency is not the absolute efficiency, rather an efficiency relative to some standard reflector. We have measured the peak transmittance through the spectrograph to be 30-35%, i.e. a little less than half the values in Figure 4.4.

The main reason for using an ICCD camera instead of other cameras with amplification, is the ability to gate the camera on and off quickly. This could also be achieved by a PMT-array, but then with significantly fewer channels. As one of the goals of this project is to investigate which requirements are critical for a fielded system, we have chosen to construct the system with relatively high performance as this would enable us to adjust down the performance to determine which is necessary.

4.2.5 System field of view

The system field of view (FOV = the range of angles from which the light enters the spectrograph through the optical system) is determined by the telescope, the slit on the input side of the spectrograph, and the optics and apertures between the telescope and the spectrograph. In our case, the size of the slit is 200 µm x 3 mm, the telescope has a 1200 m focal length and a 250 mm aperture. We have also placed a 1 mm diameter pinhole in the focal plane of the telescope in order to reduce stay light onto the detection system. The light from the telescope is collimated by an $f = 50$ mm achromatic doublet[4] and focused onto the slit by an $f = 40$ mm achromatic doublet,

[4] The reason for using a doublet and not a simple lens is that the achromatic doublet is dispersion compensated so that the focal length is constant over a large wavelength range, which is important with the large bandwidth fluorescence signal in this work.

as sketched in Figure 4.5. The choice of doublets was made to match the f-numbers of the telescope (4.8) and the spectrograph (3.6). Simple FOV calculations gives us that the FOV in the direction normal to the slit is 0.2 mrad, limited by the slit width. In the direction parallel to the slit, FOV = 0.8 mrad, limited by the aperture in the focal plane of the telescope.

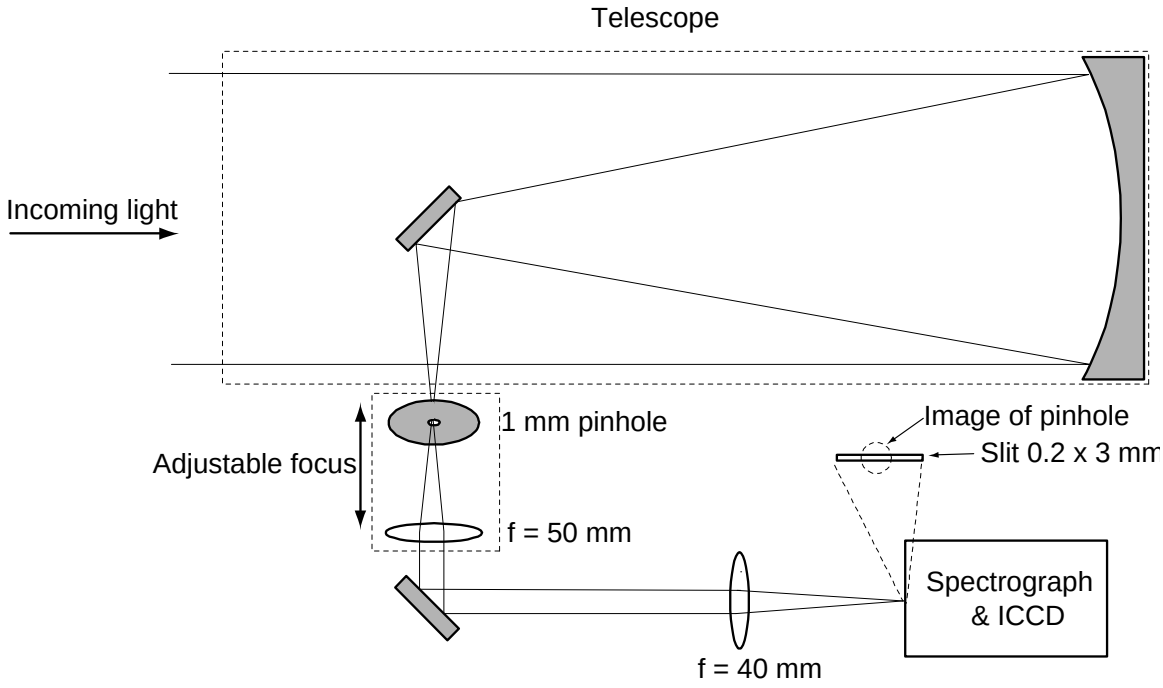

Figure 4.5 Simplified sketch of the optical path of the detection system

4.2.6 Effect of focusing/defocusing

The focal length of the telescope is 1200 mm. However, for objects that are closer than infinity, the position of the focal plane depends on the distance to the target according to the lens equation:

$$\frac{1}{f} = \frac{1}{a} + \frac{1}{b} \Rightarrow b - f = f\frac{f/a}{1 - f/a}, \tag{4.2}$$

where f is the focal length, a is the distance to the object, and b is the position of the focal plane relative to the lens. This is plotted in Figure 4.6. We observe that the position of the focal plane changes with several centimetres for distances between 50 m and 1000 m. The aperture in the focal plane of the telescope and the collimating lens should thus be adjusted to ensure maximum transmission. This adjustment is done with the ocular adjustment screw that comes with the telescope

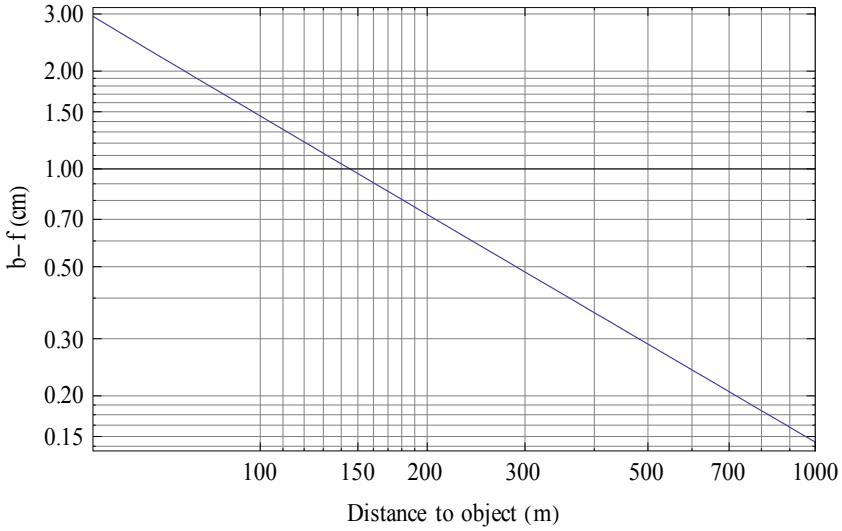

Figure 4.6 Shift of focal plane with distance to object for f=1200 mm lens

The effects of defocusing have been extensively treated in a separate report [13]. Figure 4.7 (taken from this report) shows the calculated collection efficiency as function of angle for sources located at three different distances from the telescope. The telescope is focused at 250 m distance in all simulations and the simulations were performed both with and without the 1 mm diameter limiting aperture in the telescope focal plane. We observe that the FOV is 0.2 mrad at the focal distance (the x-axis shows the half-angle), and that the FOV is "smeared" out at distances out of focus. This is especially true for 100 m distance (blue curves), at which the FOV approaches 1.5 mrad. The reason for the dip at small angles at this distance is that the secondary mirror masks the "effective" aperture at small angles. This is reduced at larger angles as an asymmetric part of the telescope is used in this instance (see [13] for a full explanation). Note that the theoretical maximum in power transmission depends on the square inverse of the distance to target, thus the maximum transmission for 100 m distance at optimal focusing is about 6 times higher than for 250 m.

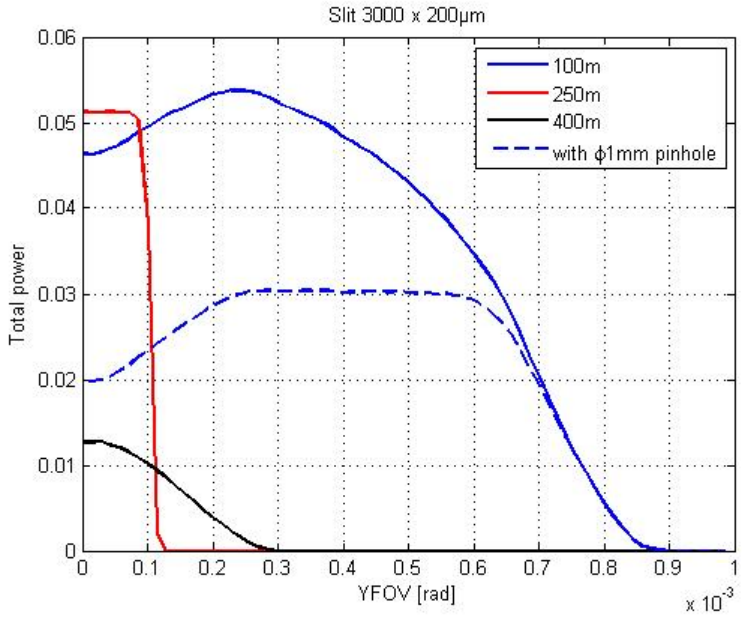

Figure 4.7 Simulated transmission through the optical system as function of incident angle for misaligned optical systems.

In this work, correct focusing has been assured by entering a CCD-camera in the optical loop and focus on objects at the desired distance, for example leaves or grass. In the field trials reported here and, more extensively, in [22], the focus was fixed at 250 m distance for practical reasons even though the distance to the clouds that were observed varied from 100 m to 450 m. As was seen in Figure 4.7, this resulted in a slightly lower throughput through the optical system for the extreme distances of this interval.

4.2.7 Summary system specifications

In Table 4.2, the biolidar specifiations are listed.

Table 4.2 Summary of biolidar specifications

Parameter	**Value**
Laser wavelength	355 nm
Laser pulse length	5 nm
Laser pulse repetition rate	10 Hz
Laser beam divergence*	0.2 x 1 mrad
Maximum pulse energy	170 mJ
Telescope diameter	250 mm
Telescope FOV	830 µrad
Spectrograph FOV*	200 x 830 µrad
Slit width	200 µm
Spectral resolution	4 nm
Camera minimum gate width	100 ns
Camera pixel size	26 µm
Camera maximum gain	500

* FWHM angle in directions normal to and parallel with the slit

The relative spectral sensitivity of the detection system was measured by recording the ambient light spectra from an overcast sky and comparing this with a simultaneous measurement performed with a calibrated spectrometer [23]. The measured sensitivity curve is shown in Figure 4.8. For comparison, a similar curve when the mirror reflecting the 355 nm radiation to the PMT was removed is also shown.

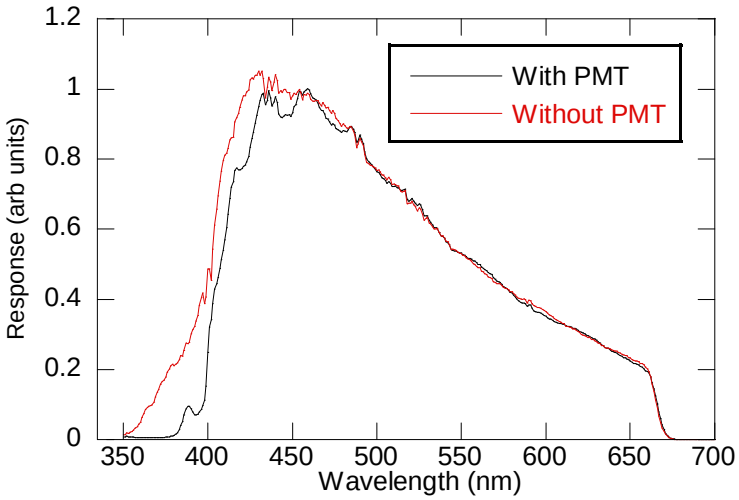

Figure 4.8 Measured spectral sensitivity curve for the biolidar detection system with and without the mirror reflecting 355 nm radiation onto the PMT

4.2.8 Alignment procedures

The alignment of the laser and telescope is crucial. In order for the telescope field of view to overlap the laser beam at all relevant distances, the two optical axes should overlap. Also, the divergence of the laser beam should match the field of view of the detection system. Moreover, the laser power has to be adjustable to compensate for distance to object as well as characteristics of the object, such as nature of fluorescence and density. For field use the instrument tilt and rotation angles have to be easily adjusted.

The laser was placed next to the telescope, and the laser beam is aligned on-axis with the field of view by two adjustable mirrors, of which the final is placed on the optical axis of the telescope. Collimation of the laser is performed by adjusting the beam expander, and the Dove-prism is rotated to make the elliptical laser far field match the geometry of the slit. Laser power reduction is carried out by means of a rotatable half-wave plate and a dielectric mirror which dumps one polarization of the beam onto a high power detector, enabling continuous monitoring of the laser power. The optical table was mounted on a tripod with manually controllable tilt and rotation.

If the lidar is operated in an environment without fluorescing aerosols, the main returns collected by the camera system is the elastic backscatter from naturally occurring aerosols as well as Raman scattering from Nitrogen, Oxygen and water vapor, as can be seen in Figure 6.2. After initial alignment of the system (i.e. aligning the emitter with the receiver) on a fluorescing background like, for example, a sheet of paper, the lidar can be fine tuned by maximizing the return on the Raman lines. This is relatively easy to perform and, since the density of N_2 in the

atmosphere is constant (at the same altitude), the return signal at the N_2-line should be constant and can be used as a systems check during experiments.

5 Laser safety

The safety limits of the 355 nm laser wavelength can be found in the IEC-60825 [24]. Since this wavelength is absorbed in water and does not penetrate the pupil of the eye, the maximum exposure limits are the same for eye and skin. The users should therefore, in addition to appropriate laser safety eyewear, wear (UV-) protective clothing.

For pulsed radiation, the maximum permissive exposure (MPE) for a single laser pulse at 355 nm with pulse length τ (in seconds) is [24, Tables 10 and A.1]

$$MPE_{\text{single pulse}} = 5.6\times10^{3}\,\tau^{0.25}\ \left[\text{J/m}^2\right]. \tag{5.1}$$

For τ = 5 ns, MPE = 4.7 mJ/cm^2. For wavelengths below 400 nm, this also applies to pulse trains[5]. The maximum output from the laser in this work is 170 mJ. Thus, the minimum safe beam area is 36 cm^2. If the beam is collimated from the lidar, this beam area occurs at approximately 140 m distance, which thus is the so-called nominal ocular hazard distance, NOHD. This only applies to the unaided eye and not to observers with e.g. binoculars. In Figure 5.1, the NOHD is shown as function of the angle of the half-wave-plate that controls the laser output energy, for different average divergence angles.

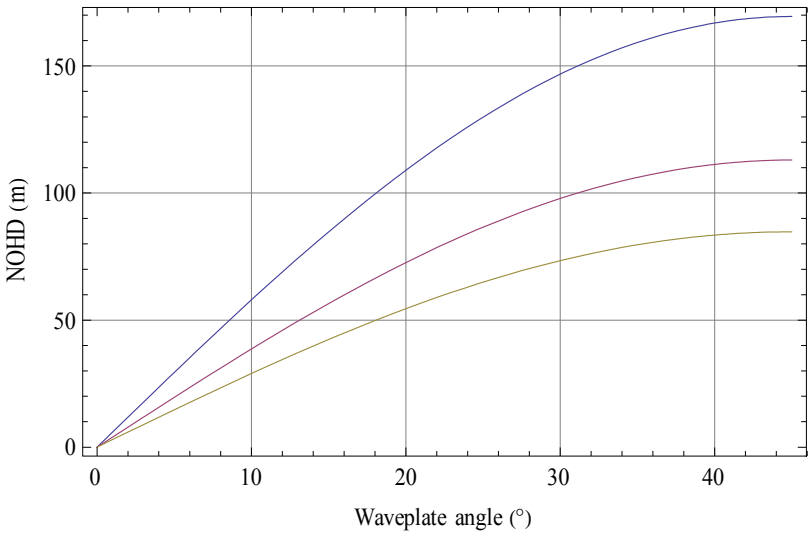

Figure 5.1 Calculated NOHD as function of angle of the half-wave-plate controlling the output laser energy (45° corresponds to 170 mJ) for 0.4, 0.6 and 0.8 mrad beam divergence (top to bottom)

[5] For wavelengths above 400 nm, the MPE is reduced by the fourth root of the number of pulses in the exposure time. A typical exposure time is 10 s, consequently the MPE is reduced by a factor of $100^{0.25}$~3.2.

6 Characterization of the lidar

6.1 Wavelength calibration

To be able to compare the spectra measured with the spectrograph and camera with a database of known spectra, it is important to calibrate the wavelength scale of the spectrograph. Optional wavelengths to calibrate this include the elastic scatter at 355 nm, the Raman-scatter from O_2 at 376 nm, N_2 at 387 nm and H_2O at 408 nm, as well as easily available laser sources at 532 nm (green), 543 nm (green) and 633 nm (red).

The spectrum recorded on the ICCD camera through the spectrograph has a linear dispersion, i.e. the wavelength is a linear function of the pixel number on the ICCD camera,

$$\lambda\left(pixel\,\#\right) = A + B \cdot pixel\,\#\ , \tag{6.1}$$

where A and B are constants. Since the spectrograph images 1:1 from the input to the exit face in the spectral direction, and the dispersion at the exit face is given as 19.9 nm/mm, constant B in the equation above should, in theory, just be given by the product of the pixel size of the ICCD and the given dispersion of the spectrograph. This leads to B = 0.5174 nm/pixel. However, when calibrating the system with all the above listed wavelengths, we found that this value is B = 0.5108 nm/pixel. Although this may seem like a small difference, the accumulated wavelength mismatch across the spectral range is 5 nm. Andor's explanation for this mismatch is that the 'pixel size' of the amplification system in front of the CCD is slightly different from the 26 µm on the CCD [25]. In the following, we thus used the measured B-value.

While B is an instrument specific constant, the constant A can be changed by alignment of the system or the angle of the grating. Thus, A should be determined frequently. It should, in theory, be sufficient to calibrate at one point. However, owing to the moderate spectral resolution of the system, we found it best to use multiple wavelengths to calibrate to reduce the wavelength uncertainty. This can be easily done during a measurement by identifying the 355 nm backscatter as well as two or three of the Raman-shifted returns, as is shown in Figure 6.1. Such calibration can also be performed in post-processing of the data, if necessary. In Figure 6.1, the peaks are at pixels 201, 239, 262 and 304. If we use the known wavelength values at these peaks and the measured B-value, we find for A: 252.0, 253.4, 252.9, 252.2. In this case, we choose to use the average value 252.6.

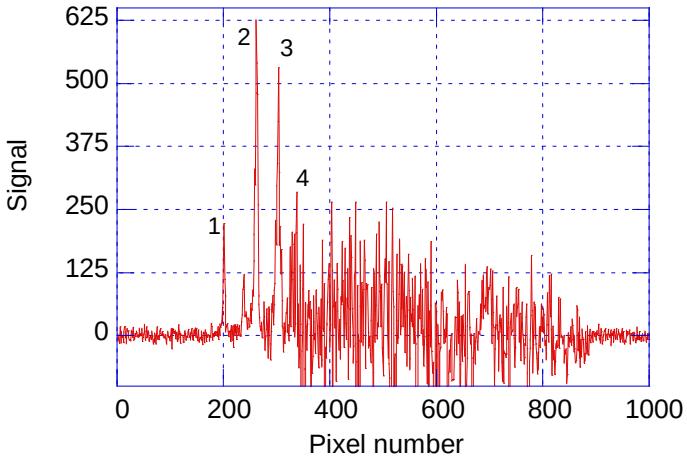

Figure 6.1 Example of a measured spectrum. Peaks labelled 1-4 are the calibration peaks discussed in the text.

6.2 Background compensation

As was indicated in Section 3.4, there is a significant incident signal from ambient light on the biolidar receiver stage. This is independent of the laser emission and should be corrected for. In Figure 6.2, an example of such an ambient signal is shown. The signal was recorded with day-light conditions with an integration time (gate width) equal to that used with the laser on.

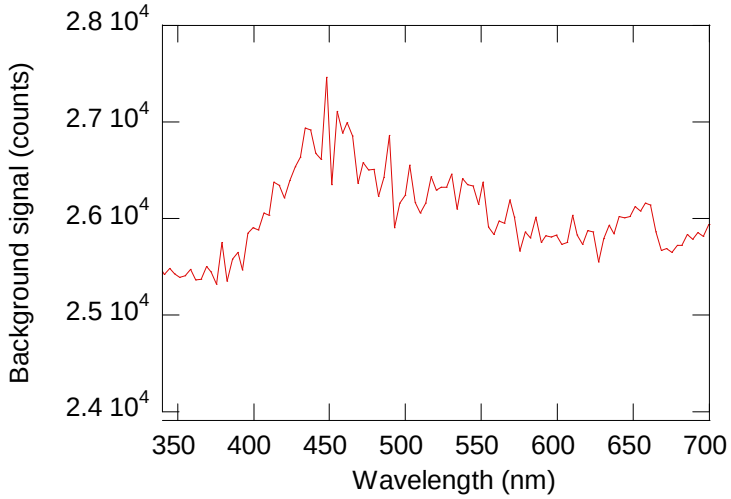

Figure 6.2 Example of signal from ambient light during a day-time recording

This ambient signal is corrected for in the recorded spectra during releases by subtracting the ambient signal recorded prior to the active measurement started, as is shown in Figure 6.3. This method worked well when the ambient light level was stable. However, if this level changed, a new recording of the ambient light level had to be performed, as is seen in Figure 6.4. This proved to be awkward under field trials, and an improved version with ambient correction on-the-fly will be implemented in the next generation control software.

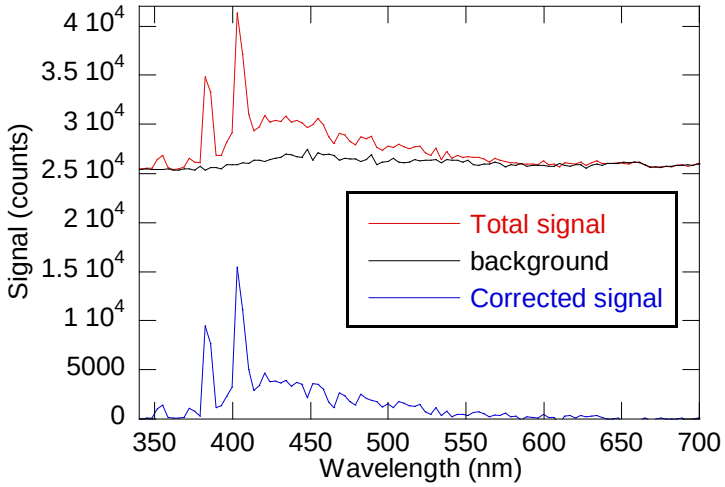

Figure 6.3 Measured signal and signal corrected for ambient light

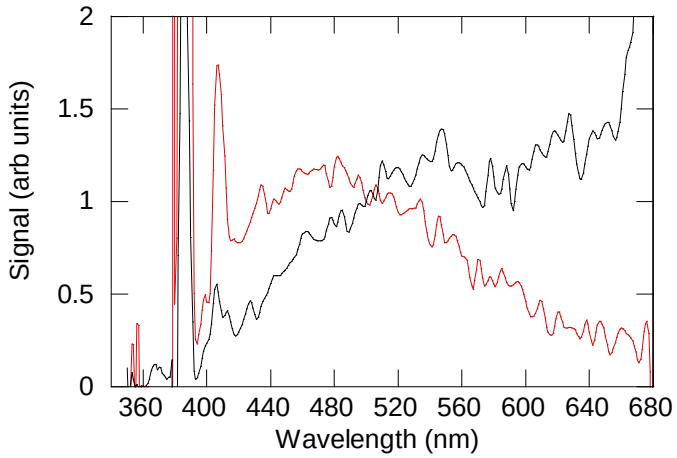

Figure 6.4 Corrected signals from an Ovalbumin release. Red curve was taken with correct ambient light correction. When the black curve was recorded, the ambient light level had increased to a higher value than was corrected for

6.3 Example of measured backgrounds and signals

In Figure 6.5, three different spectra measured with the biolidar are shown. These are for clean air (only Raman return), and the simulants *Ovalbumin* (egg white, a simulant for toxins) and *Bacillus Thuringensis* (Turex, a nonpathogenic simulant for *Bacillus Antracis*, Anthrax). A more in-depth description of the trial during which there measurements were made are found in a separate report [22].

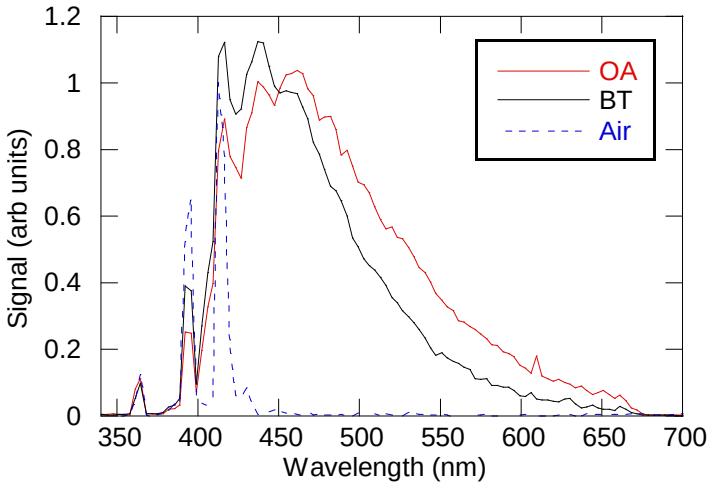

Figure 6.5 Measured biolidar returns for air, and with aerosol releases of Ovalbumin (OA) and Bacillus Thuringensis (BT)

In Figure 6.6, a typical signal on the PMT is shown for a release at ~200 m distance. The peak at 100 m distance and later drop is the return signal from the naturally occurring aerosols in the air. The reason for this to decrease at shorter distances than 100 m is that the telescope in this experiment was focused on ~250 m, and that elastic scatter at much shorter distances is not effectively collected by the optics. In the trial, a 500 m line of sight ended in a tree line. The ICCD camera was gated to avoid the fluorescence from the trees.

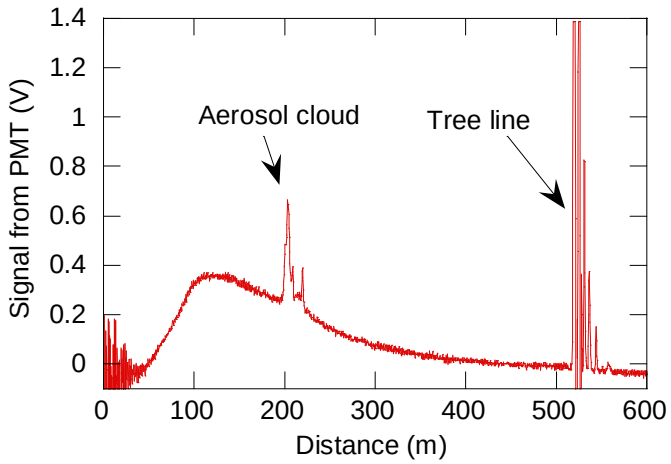

Figure 6.6 PMT signal during aerosol release at 200 m distance. The curve is explained in the text

7 Conclusions

In conclusion, the FFI biolidar has been described and the choice of components has been explained, as well as potential challenges, like operation under high ambient light conditions. The lidar uses ultraviolet laser light to induce fluorescence in aerosols with biological content, and a spectrally resolved receiver stage to measure the fluorescence spectrum. Initial testing was

performed in a field trial and demonstrated that detection of biological aerosols is possible even at daylight conditions.

The lidar was tested in a field trial in Umeå in Sweden in Novenber 2006 [22]. One of the reasons for going abroad for such test is the lack of necessary facilities in Norway. This initial trial showed that the lidar was capable of detecting biological aerosols at a distance. During this trial and subsequent work, a list of improvements to be made to the lidar was developed. This is listed in [22].

In the design of the lidar, it was chosen to keep the elements simple and – if possible – with better performance than expected necessary. This way it will be possible to reduce the performance of the lidar gradually to get an estimate of the performance needed in a final design. For example, the spectrograph and ICCD camera is clearly capable of a higher spectra resolution than necessary, but was chosen over a PMT-array with less spectral channels to be able to investigate how the number of spectral channels affects the performance of the lidar. The 355 nm laser was chosen over a 266 nm alternative because of higher available output energies and also that standard telescopes and lenses can be used to collect the 400-600 nm fluorescence following 355 nm excitation, while the shorter wavelengths emitted with 266 nm excitation require special coated mirrors and nonstandard lenses. The required spectral resolution will be subject to further study with the biolidar, and future upgrades may also include 266 nm excitation.

References

[1] Proceedings from. In: *7th Joint Conference on Standoff Detection for Chemical and Biological Defence*, (Joint Science and Technology Office, USA, 2006).

[2] Proceedings from. In: *6th Joint Conference on Standoff Detection for Chemical and Biological Defence*, (Joint Science and Technology Office, USA, 2004).

[3] *Chemical Biological Radiological Nuclear and Explosives (CBRNE) Sensing IX*. A W Fountain, ed, Proceeding of SPIE, SPIE, Bellingham, WA, USA, vol 6954, 2008.

[4] *Spectroscopy*, Encyclopædia Britannica. http://search.eb.com/eb/article-80635

[5] R M Measures. *Laser remote sensing - fundamentals and applications*. Krieger publishing company, Malabar, Florida, 1992.

[6] M Sletmoen. *Vekselvirkning mellom lys og biologisk materiale*. FFI/Notat 2008-00828 (In Norwegian), FFI, Kjeller, 2008. www.ffi.no

[7] D B Wetlaufer. Ultraviolet Spectra of Proteins and Amino Acids. *Advances in Protein Chemistry*, 17: 303-390, 1962.

[8] A T Timperman, K E Oldenburg, and J V Sweedler. Native fluorescence detection and spectral differentiation of peptides containing trypophan and tyrosine in capillary electrophoresis. *Analytical Chemistry*, 67: 3421-3426, 1995.

[9] S Pakalnis, V Sitas, H Schneckenburger, and R Rotomskis. Picosecond absorption spectroscopy of biologically active pigments NADH, FMN and fluorescence marker Rhodamine-123. In: *The Third Internet Photochemistry and Photobiology Conference*, J Photochem. Photobiol. B: Biology, (www.photobiology.com/photobiology2000, 2000).

[10] J R Simard, G Roy, P Mathieu, V Larochelle, J McFee, and J Ho. *Standoff integrated bioaerosol active hyperspectral detection (SINBAHD): Final report*. DRDC Valcartier TR 2002-125, DRDC, Valcartier, Quebec, 2003.

[11] J R Simard, G Roy, P Mathieu, V Larochelle, J McFee, and J Ho. Standoff sensing of bioaerosols using intensified range-gated spectral analysis of laser-induced fluorescence. *Ieee Transactions on Geoscience and Remote Sensing*, 42: 865-874, 2004.

[12] *Zemax*, 7.5, Bellevue, WA: Zemax development corporation, 2008. www.zemax.com

[13] S Nicolas. *Optical design for a biological lidar system*. FFI/Notat (to be published), FFI, Kjeller, 2008. www.ffi.no

[14] S Solberg, NILU, Kjeller. Personal communication. 2005

[15] *MODTRAN*, 4, Hanscom AFB, MA: Air Force Research Labs, 2008.

[16] G W Faris, R A Copeland, K Mortelmans, and B V Bronk. Spectrally resolved absolute fluorescence cross sections for Bacillus spores. *Applied Optics*, 36: 958-967, 1997.

[17] J R Stevens. *Measurements of the ultraviolet fluorescence cross sections and spectra for bacillus anthracis simulants*. ECBC-CR-004, Edgewood CBC, Aberdeen Proving Ground, MD, 1999.

[18] V Sivaprakasam, A L Huston, C Scotto, and J D Eversole. Multiple UV wavelength excitation and fluorescence of bioaerosols. *Optics Express*, 12: 4457-4466, 2004.

[19] J Kunnil, S Sarasanandarajah, E Chacko, and L Reinisch. Fluorescence quantum efficiency of dry Bacillus globigii spores. *Optics Express*, 13: 8969-8979, 2005.

[20] J R Schott. *Remote sensing: the image chain approach*. 2nd ed., Oxford University Press, New York, 2007.

[21] Andor Technology, Belfast, www.andor.com

[22] Ø Farsund and G Rustad. *Standoff detection of biologic aerosols by means of UV-laser induced fluorescence - results from Umeå trial*. FFI-rapport 2008/01990, FFI, Kjeller, 2008. www.ffi.no

[23] *FieldSpecPro Full Range User's Guide, rev C*. Analytical Spectral Devices Inc, Boulder, CO, 2002. www.asdi.com

[24] *IEC 60825-1 Safety of laser products - Part 1: Equipment classification and requirements*, Geneva: International Electrotechnical Commission, 2007.

[25] C Duncan, Andor Technology, Belfast. Personal communication. 2007

List of abbreviations

Abbreviation	Explanation
AR	Antireflection
ATP	Universal energy carrier for cells
BG	Bacillus Globii, simulant for Anthrax
BT	Bacillus Thuringensis, simulant for Anthrax
BWA	Biological Warfare Agents
CCD	Charge Coupled device, standard video camera
FOV	Field of View
ICCD	Intensified CCD, camera with gain for low light measurements
IEC	International Electrotechnical Commission, issues laser safety standards
IR	Infrared
Lidar	Light Detection and Ranging, common term for instruments using a laser to interrogate something at a distance
LIF	Laser induced fluorescence
MPE	Maximum permissible Exposure, highest safe level of laser intensity
NADH	Protein, present in synthesis of ATP and hence the metabolism in living cells
NOHD	Nominal Ocular Hazard Distance, smallest distance from laser where the intensity of the beam is below hazard level
OA, OV	Ovalbumin, egg white, simulant for toxins
PMT	Photo Multiplying Tube, detector for very weak signals
ppb	Parts per billion (10^{-9})
sr	Steradian, unit of solid angle (full sphere = 4π)
UV	Ultraviolet
UVLIF	Ultraviolet Laser Induced Fluorescence